Laminar vortex dynamics around forward-swept wings

Kai Zhang [*]
Department of Mechanical and Aerospace Engineering, Rutgers University, Piscataway, New Jersey 08854, USA

Kunihiko Taira [†]
Department of Mechanical and Aerospace Engineering, University of California, Los Angeles, California 90095, USA

(Received 5 December 2021; accepted 27 January 2022; published 9 February 2022)

Forward-swept wings offer unique advantages in the aerodynamic performance of air vehicles. However, the low-Reynolds-number characteristics of such wings have not been explored. In this work, we numerically study laminar separated flows over forward-swept wings ($\Lambda = 0^\circ$ to -45°) with semi aspect ratios sAR = 0.5–2 at a chord-based Reynolds number of 400. Forward-swept wings generate wakes that are significantly different from those of backward-swept wings. For low-aspect-ratio forward wings, the wakes remain steady due to the strong downwash effects induced by the tip vortices. For a larger aspect ratio, the downwash effects weaken over the inboard region of the wing, allowing unsteady vortex shedding to occur. A higher aspect ratio allows for the formation of streamwise vortices for highly swept wings, stabilizing the flow. Forward-swept wings can generate enhanced lift at high angles of attack compared to the unswept and backward-swept wings, with the cost of high drag. We show through force element analysis that the tip-vortex-induced downwash plays a favorable role in enhancing lift by maintaining a steady vortical structure near the tip region. With the additional vortex lift generated toward the tip of the forward-swept wing, the sectional lift is higher near the outboard region than at the inboard. This is opposite from the elliptical lift distribution for high-Reynolds-number attached flows, in which the downwash has an adverse effect on lift by reducing the effective angle of attack. The current findings offer a detailed understanding of the sweep effects on laminar separated flows over forward-swept wings, and they may pave the way for innovative designs of high-lift devices at low Reynolds numbers.

DOI: 10.1103/PhysRevFluids.7.024704

I. INTRODUCTION

Low-Reynolds-number aerodynamics of finite-aspect-ratio lifting surfaces have been widely studied for developing micro air vehicles and understanding biological flights. The wakes of these small-scale wings embody rich flow physics comprised of unsteady separation, vortex formation, and wake interactions, which are influenced by such factors as Reynolds number and platform shape [1–3]. The sweep angle has also been shown to play a key role in shaping the wake dynamics [4–7]. Most of these studies have focused on backward-swept wings.

Forward-swept wings, although less common in air vehicle designs, offer unique advantages that make them suitable for agile flights at high angles of attack. In general, swept wings have the

[*]Present address: School of Naval Architecture, Ocean and Civil Engineering, Shanghai Jiao Tong University, Shanghai 200240, China; kai.zhang@sjtu.edu.cn
[†]ktaira@seas.ucla.edu

 ©2022 American Physical Society

property that their aft sections stall first. In conventional backward-swept wings, stall occurs first near the wing tip [5,7,8], resulting in a loss of aileron control. For forward-swept wings, since stall commences at the inboard region, ailerons can still be effective at high angles of attack to offer high maneuverability. This feature has been demonstrated by the Grumman X-29 experimental aircraft, which gave pilots excellent control response up to a 45° angle of attack [9]. In addition, many aerial animals have been observed to sweep their wings forward during slow flights because the wings are required to operate at high angles of attack providing high lift to support body weight [10]. Many species also exhibit forward wings during high angle-of-attack perching and snatching maneuvers [11].

The aerodynamic benefits of forward-swept wings have attracted a number of studies on their wake characteristics. Breitsamter and Laschka [12] conducted extensive experimental investigations on the flows over forward-swept wings at $\mathrm{Re} = 4.6 \times 10^5$. They observed that the wing tip vortex and the leading edge vortex with an opposite sense of rotation dominate the flow field. The leading-edge vortex can burst at moderate angles of attack in the outer wing region. Traub and Lawrence [13] studied these flows over a thin 65° swept wing in forward and backward sweep configurations, both revealing vortex-dominated flows. Surface flow visualization showed large extents of flow separation near the wing root of the forward-swept wings, which feature significantly lower lift compared to the backward-swept wings. Lee and Ko [14] measured the near-field tip-vortex flow behind a forward-swept wing at $\mathrm{Re} = 1.74 \times 10^5$. Recently, Setoguchi and Kanazaki [15] investigated the separated vortical flows from the forward-swept wings at low speed and high angle of attack conditions through Reynolds-averaged Navier-Stokes simulations. They asserted that forward-swept wings exhibit benefits in terms of stall characteristics, since separated vortices remain on the outboard wing up to high angles of attack.

The above studies have discussed the aerodynamic characteristics of forward-swept wings at relatively high Reynolds numbers. However, a detailed characterization of the three-dimensional wake dynamics of forward-swept wings at low Reynolds number remains unexplored. The low-Re flows can be significantly different from their high-Re counterparts, due to increased viscous effects that promote flow separation. In addition, the three-dimensional end effects of finite-aspect-ratio wings further complicate the wake dynamics by inducing nonlinear vortex interactions, which are beyond conventional high-speed aerodynamics theories [3,16,17]. A thorough understanding of the laminar wake dynamics of forward-swept wings is of fundamental importance to the low-speed aerodynamics community. The insights obtained from such study not only lay the foundation for interpreting more complex flows at higher Reynolds numbers and those with unsteady wing motions, but they can also inspire novel designs of small-scale high-lift devices.

In this work, we perform a large number of direct numerical simulations to study the three-dimensional separated flows over forward-swept finite-aspect-ratio wings at a Reynolds number of 400. The present study, together with our previous work on backward-swept wings [7], offers a comprehensive coverage of sweep effects on separated flows over finite-aspect-ratio wings. In what follows, we present the computational setup and its validation in Sec. II. The results are discussed in Sec. III, where we provide descriptions of the wake vortical structures and the aerodynamic forces. We also present a force element analysis to identify key wake structures that are responsible for lift generation. We conclude this study by summarizing our findings in Sec. IV.

II. COMPUTATIONAL SETUP

We study the incompressible flows over finite-aspect-ratio forward-swept wings with a NACA 0015 cross section. A schematic of the wing is shown in Fig. 1. The wings are subjected to uniform flow with velocity U_∞ in the x direction. The z axis aligns with the spanwise direction of the unswept wing, and the y axis points in the direction of lift. The sweep angle Λ is defined as the angle between the z axis and the leading edge. The symmetry boundary condition is prescribed along the midspan. Denoting half wing span as b, the semi aspect ratio is defined as $\mathrm{sAR} = b/c$, where c is the chord length. The Reynolds number, defined as $\mathrm{Re} \equiv U_\infty c/\nu$ (ν is the kinematic viscosity of the fluid), is

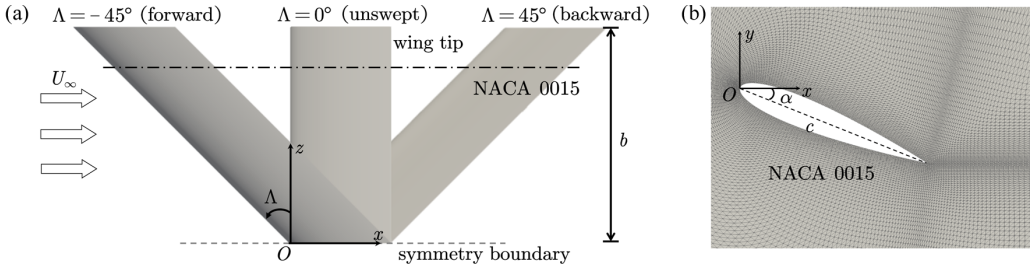

FIG. 1. (a) Case setup for flows over swept wings, and (b) grid setup in the vicinity of the wing.

fixed at 400. In what follows, all the spatial variables are normalized by the chord length c, velocity by U_∞, and time by c/U_∞. The lift and drag coefficients are defined as $C_L = F_L/(\rho U_\infty^2 bc/2)$ and $C_D = F_D/(\rho U_\infty^2 bc/2)$, where F_L and F_D are the aerodynamic forces exerted on the semispan wing in the y and x directions, respectively, and ρ is the fluid density.

The finite-volume-based flow solver PIMPLEFOAM of the OPENFOAM toolbox [18] is used to simulate the flows with second-order spatial and temporal accuracy. We employed a C-type grid with mesh refined in the vicinity of the wing as well as its wake, as shown in Fig. 1(b). For the swept cases, the mesh is sheared toward the streamwise direction along with the wing. Such a grid setup is similar to our previous works [7,19], for which a commercial CFD code CLIFF (CHARLES package) was used [20,21]. In our previous study, the numerical setup of CLIFF was validated with results from companion water tunnel experiments [19]. To validate the present results from OPENFOAM, we compare the force coefficients of the unswept wing $(\mathrm{sAR}, \alpha, \Lambda) = (2, 20°, 0°)$ and the backward-swept wing $(\mathrm{sAR}, \alpha, \Lambda) = (2, 20°, 45°)$ computed from CLIFF and PIMPLEFOAM in Figs. 2(a) and 2(b). The time traces of the forces obtained from the two solvers agree well with each other, and their time-averaged values differ less than 1%. In addition, the vortical structures of the backward-swept wing computed from both solvers match very well, as shown in Fig. 2(c), validating the present computational results.

III. RESULTS

A. Wake vortical structures

The wake vortical structures behind high-incidence forward-swept wings can take three major forms, as shown in Fig. 3. These wakes are classified as (a) steady flow due to tip vortices (▲),

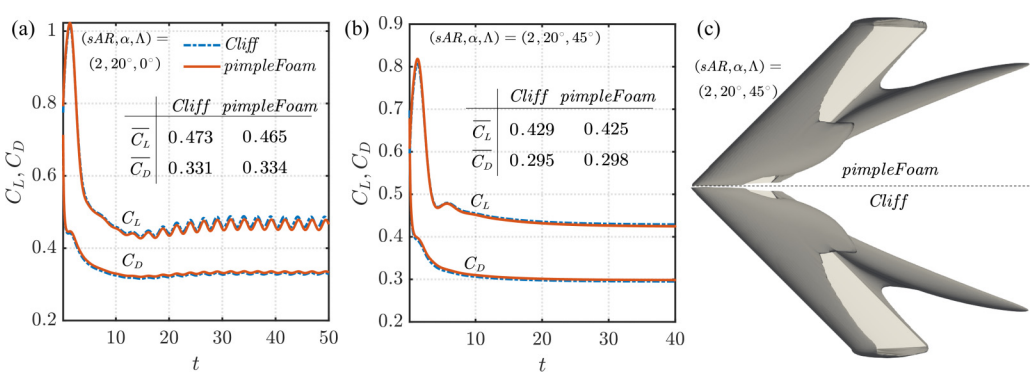

FIG. 2. Comparisons of force coefficients (a), (b) and wake vortical structures (c) computed from CLIFF and PIMPLEFOAM for $(\mathrm{sAR}, \alpha, \Lambda) = (2, 20°, 0°)$ and $(\mathrm{sAR}, \alpha, \Lambda) = (2, 20°, 45°)$. The inset tables in (a), (b) summarize the time-averaged force coefficients $\overline{C_L}$ and $\overline{C_D}$. The vortical structures in (c) are visualized with isosurfaces of $Qc^2/U_\infty^2 = 1$, where Q is the second invariant of the velocity gradient tensor.

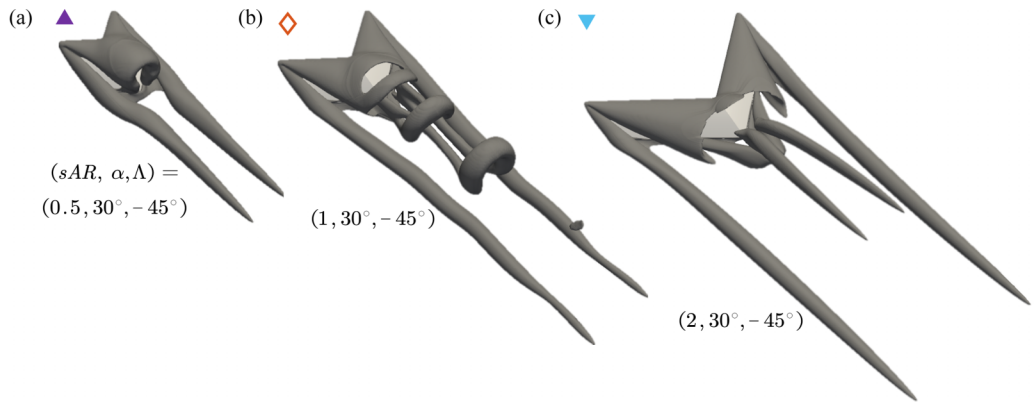

FIG. 3. Representative wake vortical structures for forward-swept wings, visualized by isosurfaces of $Qc^2/U_\infty^2 = 1$.

(b) unsteady vortex shedding near the midspan (◇), and (c) steady flow with streamwise vortices (▼). We map out these flows over the Λ-α space for different aspect ratios in Fig. 4, in which the backward-swept wing wakes [7] are also included. The wakes for $\alpha \leqslant 12^\circ$ are clustered into one group as they are steady at Re $= 400$ regardless of aspect ratio and sweep angle.

The most prominent feature of the forward-swept wing wakes is the presence of the tip vortices, as shown in Fig. 3. In comparison, the tip vortices can be suppressed for backward-swept wings. This is due to the outboard spanwise flow induced by the backward-swept wing that counteracts the roll-up of flow around the tip [7]. With increasing forward sweep angle, the tip vortices grow stronger with increasing forward sweep angle, as observed in Fig. 4. The wake dynamics of low-aspect-ratio forward-swept wings are significantly influenced by the tip vortices.

At sAR $= 0.5$, the tip vortices induce strong downwash effects over the entire span of the wings, acting to suppress the shedding of the leading-edge vortex sheet [7,19,22,23]. As a result, the wakes of forward-swept wings with sAR $= 0.5$ are mostly steady, as shown in Fig. 4(a). The leading-edge vortex sheet rolls up near the midspan into a domelike shape. It is not until $\alpha = 30^\circ$ that the unsteady vortex shedding emerges. The forward-swept wing can achieve steady flow at smaller sweep angle than the backward-swept case, as the former is subjected to stronger downwash effects from the tip vortices.

For higher-aspect-ratio forward-swept wings, the downwash induced by the tip vortex becomes weaker near the midspan, allowing the detachment of the leading-edge vortex sheet. The flow thus features unsteady vortex shedding, as shown in Fig. 3(b). This type of flow prevails for high-incidence forward-swept wings with sAR $= 1$, as shown in Fig. 4(b). The stability boundary in the Λ-α space at sAR $= 1$ is asymmetric with respect to $\Lambda = 0$, with the backward-swept wings exhibiting steady flows over a larger region of the parameter space. These steady flows of backward-swept wings are achieved due to the formation of a pair of vortical structures near the midspan on the suction side, which impose downward velocity to each other and stabilize the wake [7], as schematically shown in Fig. 5. In the forward-swept case, such induced velocity from the root vortical structures poses an uplifting effect on each other, promoting vortex shedding near midspan. The midspan effects of backward-swept wings are localized to the inboard region of the span. For cases with a large angle of attack and a higher aspect ratio, the backward-swept wings generate unsteady vortex shedding near the tip region, which is not observed for forward-swept wings.

For sAR $= 2$, the increased span allows for the formation of streamwise vortices (in addition to the tip vortices) over the inboard region, acting as a wake-stabilizing mechanism for both forward- and backward-swept wings with high sweep angles. For the forward-swept wings, two pairs of such

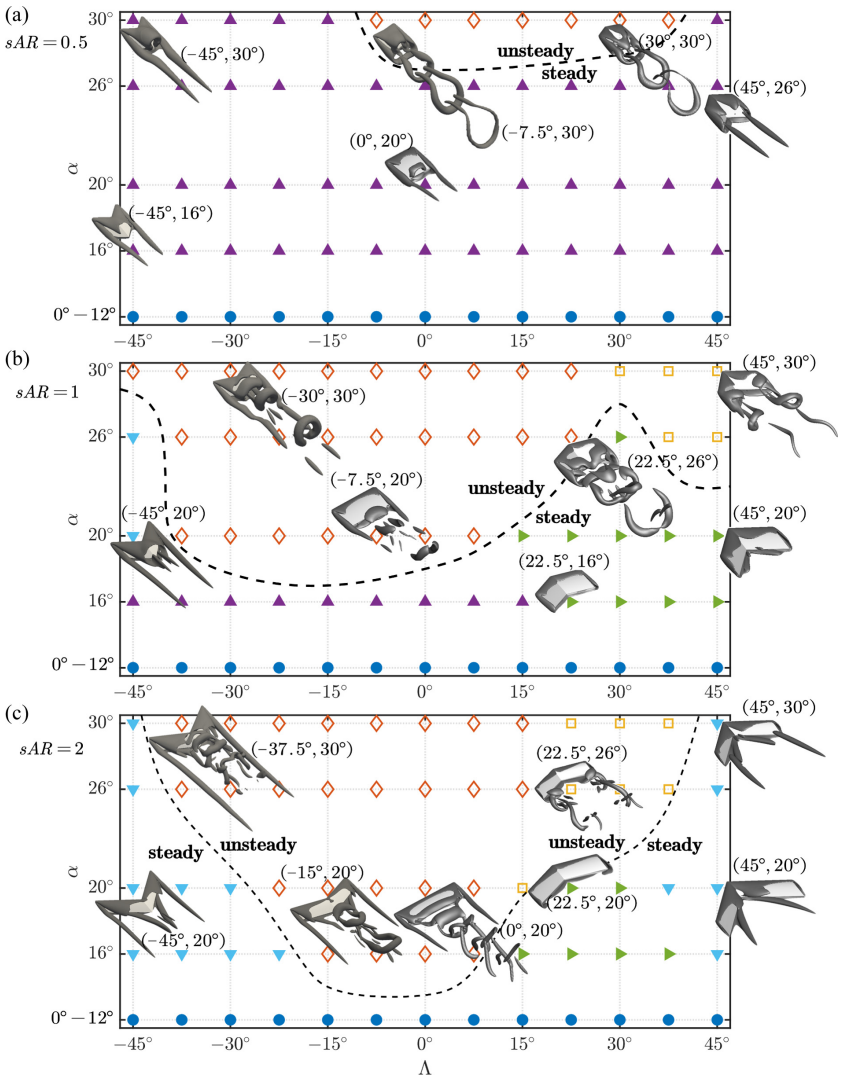

FIG. 4. Classification of wake vortical structures behind swept wings for (a) sAR = 0.5, (b) sAR = 1, and (c) sAR = 2. ▲: steady flow due to tip effects; ◇: unsteady shedding near midspan; ▶: steady flow due to midspan effects; □: unsteady shedding near wing tip; ▼: steady flow with streamwise vortices. ●: steady flow due to low Re. The dashed lines delineate the approximate boundaries between steady (filled symbols) and unsteady (empty symbols) flows. The vortical structures are visualized by isosurfaces of $Qc^2/U_\infty^2 = 1$ for representative cases. The values in the parentheses (Λ, α) denote the sweep angle and angle of attack for the shown snapshot insets.

streamwise vortices are observed for the sAR = 2 wings. The first pair resides in the near wake of the midspan region, and they appear detached from the rest of the vortical structures, as shown in the inset diagram for $(\Lambda, \alpha) = (-45^\circ, 20^\circ)$ in Fig. 4(b). The other pair on the trailing edge grows from the tip region and contracts towards the midspan. This set of streamwise vortices is similar to those found in the backward-swept cases, in which the streamwise vortices grow from midspan and trail toward the tip [7]. This difference reflects the reverse of the spanwise flow as the wings are swept from backward to forward. The stability boundary at sAR = 2 in the Λ-α space appears almost

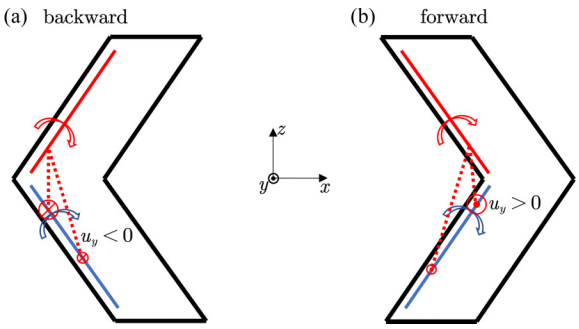

FIG. 5. A schematic of the induced velocity near midspan of (a) backward- and (b) forward-swept wings. The red and blue solid lines represent the vorticity lines generated from the leading edges (in the absence of end effects). In the case of backward-swept wings, the red vorticity line generates downward induced velocity ($u_y < 0$) on the blue line. For forward-swept wings, the induced velocity points upward ($u_y > 0$), promoting unsteady shedding.

symmetric for forward- and backward-swept wings. These steady streamwise vortices observed in the large-aspect-ratio swept wings resemble those found in the wakes of inclined slender bodies with inhomogeneous end boundary conditions, where the impulsively started flow analogy can be invoked to understand their formation mechanism [19,24,25].

B. Aerodynamic forces and moments

The time-averaged aerodynamic force coefficients $\overline{C_L}$, $\overline{C_D}$, the lift-to-drag ratio $\overline{C_L/C_D}$, and the pitch coefficient $\overline{C_M}$ of the swept wings are shown in Fig. 6. Here, the pitch moment coefficient is defined as $C_M = M/(\rho U_\infty^2 bc^2/2)$, where M is the half-span pitch moment about the quarter-chord line on the midsection ($z = \mathrm{sAR}/2$) between the tip and the root planes, and positive M acts to pitch the wing in the nose-up direction. For the lift coefficients shown in Fig. 6(a), the inviscid lift limit of finite-aspect-ratio unswept wings calculated with $C_L = 2\pi\alpha/(\sqrt{1 + (1/\mathrm{sAR})^2} + 1/\mathrm{sAR})$ is shown [26].

The lift coefficients increase almost linearly for low angles of attack ($\alpha \lesssim 12^\circ$). The introduction of forward sweep has a negative impact on $\overline{C_L}$ across different aspect ratios for these low-incidence wings, while backward sweep can enhance lift for the sAR = 0.5 and 1 wings. On the other hand, at high angles of attack ($\alpha \gtrsim 20^\circ$), the forward-swept wings generally feature higher $\overline{C_L}$ than the backward-swept and unswept wings. This phenomenon is associated with a strong downwash effect provided by the tip vortices in forward-swept wings, which will be discussed in Sec. III C.

The drag coefficients shown in Fig. 6(b) generally exhibit a quadratic growth with the angle of attack over the studied range. At low angles of attack, the drag coefficients remain close to each other among wings with different sweep angles. At high α, accompanying the high lift of forward-swept wings, $\overline{C_D}$ also increases with forward sweep angle. As a result, the lift-to-drag ratios of the forward-swept wings are generally smaller than the backward-swept cases, as shown in Fig. 6(c).

The pitch moments for both the forward- and backward-swept wings are positive, and increase with the angle of attack monotonically, as shown in Fig. 6(d). This suggests an inherent pitch instability with nose-up motion of the swept wings around their midsections. As the aspect ratio increases, the difference in pitch moments among cases with different sweep angle enlarges. The pitch moments of forward-swept wings are generally smaller than the backward-swept cases for wings with larger aspect ratios. In particular, for sAR = 2, both the forward- and backward-swept wings feature higher pitch moments than the unswept cases, indicating highly uneven force distributions along the wing span.

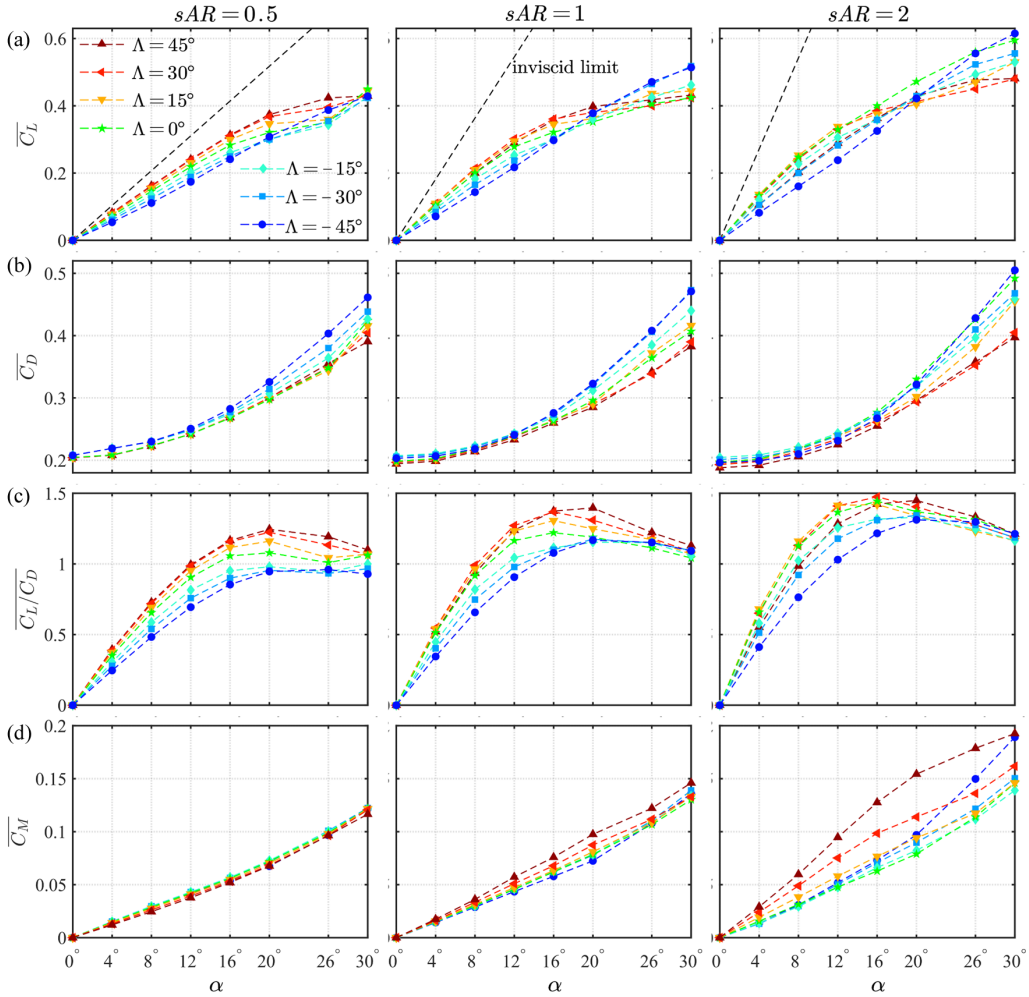

FIG. 6. Time-averaged aerodynamic force coefficients of forward-swept wings. (a) Lift coefficient $\overline{C_L}$; (b) drag coefficient $\overline{C_D}$; (c) lift-to-drag ratio $\overline{C_L/C_D}$, and (d) pitch coefficient $\overline{C_M}$ about the quarter chord on the midsection between tip and root planes. The black dashed lines in the $\overline{C_L}$ plots represent the inviscid limit for unswept wings. Left, middle, and right columns show data for sAR = 0.5, 1, and 2, respectively.

The sectional lift and drag coefficients for both forward- and backward-swept wings with $(\mathrm{sAR}, \alpha) = (2, 20^\circ)$ are shown in Fig. 7. As discussed in Ref. [7], the backward-swept wings feature higher sectional lift at the inboard region, where a pair of vortical structures are formed on the suction side due to the three-dimensional midspan effects. For the forward-swept wings, the sectional lift increases from inboard to around half a chord away from the tip, and then it decreases drastically towards the tip. The high lift near the wing tip of forward-swept wings complements the low sectional lift in the inboard region, and it could lead to an overall increase in lift for low-aspect-ratio wings, as discussed with regard to Fig. 6(a). The fact that the sectional lift is higher at the upwind end of the wing span (tip for forward-swept wing, and root for backward-swept wing) also explains the positive pitch moments for both wings.

We note that the lift distributions of both forward- and backward-swept wings in laminar separated flows are different from their counterparts in high-Re attached flows. As shown in the inset in Fig. 7(a), for high-Re flows, the sectional lift of forward-swept wings follows an elliptical

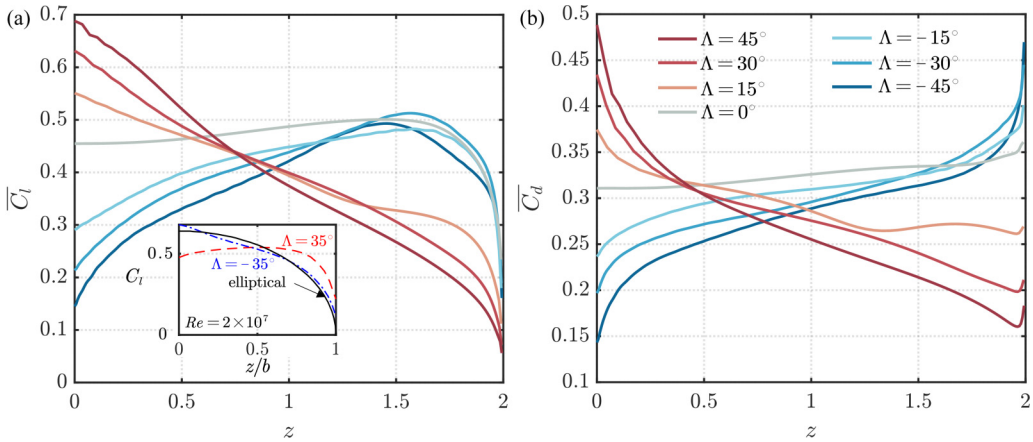

FIG. 7. Sectional force distributions for (sAR, α) = (2, 20°) wings with different sweep angles. (a) Sectional lift coefficients. The inset shows the lift distributions of forward- and backward-swept wings operating at Re = 2×10^7 [27,28]. (b) Sectional drag distribution.

distribution due to the reduced effective angle of attack by tip-vortex-induced downwash [27,28]. However, as will be demonstrated in Sec. III C, the downwash effect plays a positive role of enhancing lift in low-Re separated flows, as discussed previously. The backward-swept wing in high-Re flow features higher lift at outboard [5,29], while the opposite is true in the low-Re case. These disparities highlight significant differences between the current vortex-dominated flows compared to the high-Re attached flows.

The drag coefficients of the forward- and backward-swept wings exhibit inverse distribution along the wing span. In the former case, the sectional drag increases with the spanwise location and finishes with a surge towards the tip, while in the latter case, the highest sectional drag is found at the most inboard section. The higher sectional lift and drag in the outboard region of forward-swept wings lead to increased bending moments at the root plane, calling for reinforced structural design.

C. Force element analysis

We use the force element theory [30] to identify the flow structures that are responsible for exerting aerodynamic forces on the wing, and we explain the distinct lift distributions between forward- and backward-swept wings. This theory has also been derived in several related forms, and referred to as the variational approach [31,32], reciprocal theorem [33], vortex force maps [34], and the force partition method [35]. To apply this theory, we compute an auxiliary potential function ϕ_L (satisfying $\nabla^2\phi_L = 0$) with the boundary condition $-\boldsymbol{n}\cdot\nabla\phi_L = \boldsymbol{n}\cdot\boldsymbol{e_y}$ on the wing surface ($\boldsymbol{e_y}$ is the unit vector in the lift direction). By taking the inner product of the momentum equation for incompressible flow with $\nabla\phi_L$ and integrating over the entire fluid domain V, the lift force can be recovered as

$$F_L = \int_V \boldsymbol{\omega}\times\boldsymbol{u}\cdot\nabla\phi_L dV + \frac{1}{\mathrm{Re}}\int_{\partial V}\boldsymbol{\omega}\times\boldsymbol{n}\cdot(\nabla\phi_L + \boldsymbol{e_y})dS. \tag{1}$$

The integrands in the first and second terms on the right-hand side of this equation are the volume and the surface lift elements, respectively. At Re = 400, the volume force elements contribute more significantly to the total force than the surface force elements.

We present the lift elements for forward-swept (sAR, α, Λ) = (2, 20°, −45°) and backward-swept wings (sAR, α, Λ) = (2, 20°, 45°) on the isosurfaces of $Qc^2/U_\infty^2 = 1$ in Fig. 8. In general, the vortex sheets emanating from both the leading and trailing edges are associated with positive

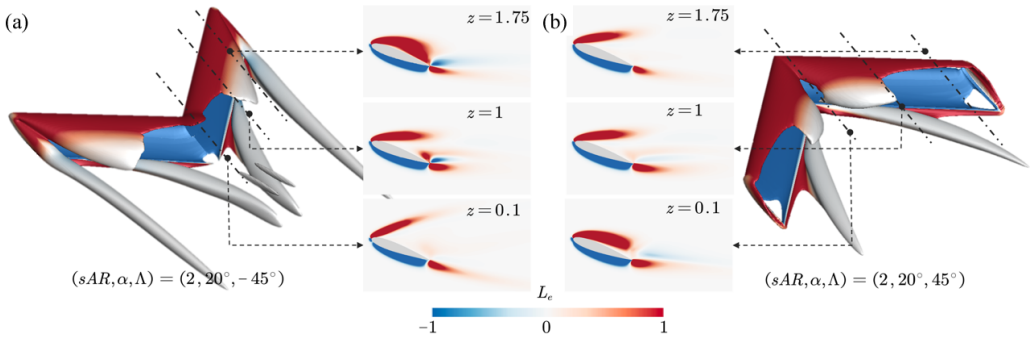

FIG. 8. Lift elements for (a) forward-swept wing (sAR, α, Λ) = (2, 20°, −45°) and (b) backward-swept wing (sAR, α, Λ) = (2, 20°, 45°). The lift elements from −1 (blue) to 1 (red) are plotted on the isosurfaces of $Qc^2/U_\infty^2 = 1$. The sectional slices show color maps of $L_e \in [-1, 1]$ at different spanwise locations.

lift, while the flow near the pressure side of the wing contributes to negative lift [36]. For the forward-swept wing shown in Fig. 8(a), the positive lift elements on the suction side of the wing appear thicker and closer to the wing surface towards the tip than those in the inboard regions. This is due to the strong tip-vortex-induced downwash effects that confine vorticity to the vicinity of the wing, as discussed in Sec. III A. On the other hand, the backward-swept wing enhances lift through the formation of a pair of vortical structures near the midspan, where the concentrated lift elements are attached to the wing surface [7]. These observations of the force elements in forward- and backward-swept wings explain their distinct lift distributions, as discussed in Fig. 7. Despite the different mechanisms in maintaining the steady vortical structures on the suction sides of the wings, both forward- and backward-swept wings are able to harness separated flows to generate additional vortical lift at high incidence, thus enhancing their aerodynamic performance.

IV. CONCLUSIONS

We have performed three-dimensional direct numerical simulations to study the effects of forward sweep on the wake dynamics and aerodynamic characteristics of finite-aspect-ratio wings at a chord-based Reynolds number of 400, covering aspect ratios of sAR = 0.5–2, angles of attack $\alpha = 0^\circ$–30°, and sweep angle $\Lambda = 0^\circ$ to -45°. The flows over forward-swept wings generally feature a pair of counter-rotating tip vortices, which shapes the wake dynamics significantly. For low-aspect-ratio forward-swept wings, the wakes are strongly influenced by the tip-vortex-induced downwash effects and they remain steady. With increasing aspect ratio, the downwash effects weaken over the inboard regions of the wing, resulting in unsteady vortex shedding. For wings with higher forward-sweep angles, streamwise vortices develop in the wake, again stabilizing the flow.

The forward-swept wings can experience enhanced lift from the separated flows at high angles of attack. This comes at the cost of high drag, which results in lower lift-to-drag ratios for forward-swept wings. We show that the high lift of forward-swept wings is mainly contributed from the outboard region of the span, where the tip-vortex-induced downwash maintains a steady vortical structures that provides additional vortex lift. This observation is different from the scenario in high-Re attached flows, where the sectional lift displays an elliptical distribution due to the reduced effective angle of attack by downwash. Together with our previous studies on backward-swept wings, the present results provide a comprehensive understanding of the sweep effects on the laminar separated flows over finite-aspect-ratio wings, and they offer coverage of the less explored area of the low-Re aerodynamic database.

ACKNOWLEDGMENTS

K.Z. is grateful to the Office of Advanced Research Computing (OARC) at Rutgers, The State University of New Jersey for providing access to the Amarel cluster. K.T. acknowledges support from the U.S. Air Force Office of Scientific Research (Grants No. FA9550-17-1-0222 and No. FA9550-22-1-0174).

The authors report no conflict of interest.

[1] T. J. Mueller and J. D. DeLaurier, Aerodynamics of small vehicles, Annu. Rev. Fluid Mech. **35**, 89 (2003).

[2] J. Winslow, H. Otsuka, B. Govindarajan, and I. Chopra, Basic understanding of airfoil characteristics at low Reynolds numbers ($10^4 - 10^5$), J. Aircr. **55**, 1050 (2018).

[3] J. D. Eldredge and A. R. Jones, Leading-edge vortices: Mechanics and modeling, Annu. Rev. Fluid Mech. **51**, 75 (2019).

[4] D. Küchemann, Types of flow on swept wings—with special reference to free boundaries and vortex sheets, tech. note aero 2234 (Royal Aircraft Establishment, 1953).

[5] C. W. Harper and R. L. Maki, A review of the stall characteristics of swept wings, tech. note d-2373 (NASA, 1964).

[6] M. R. Visbal and D. J. Garmann, Effect of sweep on dynamic stall of a pitching finite-aspect-ratio wing, AIAA J. **57**, 3274 (2019).

[7] K. Zhang, S. Hayostek, M. Amitay, A. Burtsev, V. Theofilis, and K. Taira, Laminar separated flows over finite-aspect-ratio swept wings, J. Fluid Mech. **905**, R1 (2020).

[8] J. Black, Flow studies of the leading edge stall on a swept-back wing at high incidence, Aeronaut. J. **60**, 51 (1956).

[9] T. W. Putnam, X-29 flight research program, technical memorandum 86025 (NASA, 1984).

[10] A. L. R. Thomas and G. K. Taylor, Animal flight dynamics I: Stability in gliding flight, J. Theor. Biol. **212**, 399 (2001).

[11] Z. R. Manchester, J. I. Lipton, R. J. Wood, and S. Kuindersma, A variable forward-sweep wing design for enhanced perching in micro aerial vehicles (AIAA Paper 2017-0011, 2017).

[12] C. Breitsamter and B. Laschka, Vortical flowfield structure at forward swept-wing configurations, J. Aircr. **38**, 193 (2001).

[13] L. W. Traub and J. Lawrence, Aerodynamic characteristics of forward and aft swept arrow wings, J. Aircr. **46**, 1454 (2009).

[14] T. Lee and L. S. Ko, Vortex wake generated behind a forward swept wing, J. Aircr. **46**, 717 (2009).

[15] N. Setoguchi and M. Kanazaki, Low-speed and high angle of attack aerodynamic characteristics of supersonic business jet with forward swept wing (AIAA Paper 2020-0534, 2020).

[16] J. Katz and A. Plotkin, *Low-speed Aerodynamics* (Cambridge University Press, Cambridge, 2001).

[17] W. Shyy, Y. Lian, J. Tang, D. Viieru, and H. Liu, *Aerodynamics of Low Reynolds Number Flyers* (Cambridge University Press, Cambridge, 2008).

[18] H. G. Weller, G. Tabor, H. Jasak, and C. Fureby, A tensorial approach to computational continuum mechanics using object-oriented techniques, Comput. Phys. **12**, 620 (1998).

[19] K. Zhang, S. Hayostek, M. Amitay, W. He, V. Theofilis, and K. Taira, On the formation of three-dimensional separated flows over wings under tip effects, J. Fluid Mech. **895**, A9 (2020).

[20] F. Ham and G. Iaccarino, Energy conservation in collocated discretization schemes on unstructured meshes, Annual Research Briefs (Center for Turbulence Research, Stanford University, 2004), pp. 3–14.

[21] F. Ham, K. Mattsson, and G. Iaccarino, Accurate and stable finite volume operators for unstructured flow solvers, Annual Research Briefs (Center for Turbulence Research, Stanford University, 2006), pp. 243–261.

[22] K. Taira and T. Colonius, Three-dimensional flows around low-aspect-ratio flat-plate wings at low Reynolds numbers, J. Fluid Mech. **623**, 187 (2009).

[23] A. C. DeVoria and K. Mohseni, On the mechanism of high-incidence lift generation for steadily translating low-aspect-ratio wings, J. Fluid Mech. **813**, 110 (2017).
[24] T. Sarpkaya, Separated flow about lifting bodies and impulsive flow about cylinders., AIAA J. **4**, 414 (1966).
[25] K. D. Thomson and D. F. Morrison, The spacing, position and strength of vortices in the wake of slender cylindrical bodies at large incidence, J. Fluid Mech. **50**, 751 (1971).
[26] H. B. Helmbold, Der unverwundene ellipsenflugel als tragende flanche, Jahrbuch 1942 der Deutch Luftfahrtforsch (1942), pp. I111–I113.
[27] S. Gudmundsson, *General Aviation Aircraft Design Applied Methods and Procedures* (Butterworth-Heinemann, Waltham, MA, 2013).
[28] R. Vos and S. Farokhi, *Introduction to Transonic Aerodynamics* (Springer, Dordrecht, Netherlands, 2015).
[29] K. Nickel and M. Wohlfahrt, *Tailless Aircraft in Theory and Practice*, AIAA Education Series (AIAA, Reston, VA, 1994).
[30] C. C. Chang, Potential flow and forces for incompressible viscous flow, Proc. R. Soc. London A **437**, 517 (1992).
[31] L. Quartapelle and M. Napolitano, Force and moment in incompressible flows, AIAA J. **21**, 911 (1983).
[32] B. Protas, A. Styczek, and A. Nowakowski, An effective approach to computation of forces in viscous incompressible flows, J. Comput. Phys. **159**, 231 (2000).
[33] J. Magnaudet, A reciprocal theorem for the prediction of loads on a body moving in an inhomogeneous flow at arbitrary reynolds number, J. Fluid Mech. **689**, 564 (2011).
[34] J. Li, X. Zhao, and M. Graham, Vortex force maps for three-dimensional unsteady flows with application to a delta wing, J. Fluid Mech. **900**, A36-1 (2020).
[35] K. Menon and R. Mittal, Quantitative analysis of the kinematics and induced aerodynamic loading of individual vortices in vortex-dominated flows: a computation and data-driven approach, J. Comput. Phys. **443**, 110515 (2021).
[36] K. Menon and R. Mittal, Significance of the strain-dominated region around a vortex on induced aerodynamic loads, J. Fluid Mech. **918**, R3-1 (2021).